The 2010 IEEE/RSJ International Conference on
Intelligent Robots and Systems
October 18-22, 2010, Taipei, Taiwan

Human Arm Impedance: Characterization and Modeling in 3D Space

Panagiotis K. Artemiadis, Pantelis T. Katsiaris, Minas V. Liarokapis, and Kostas J. Kyriakopoulos

Abstract— **Humans perform a wide range of skillful and dexterous motion by adjusting the dynamic characteristics of their musculoskeletal system during motion. This capability is based on the non-linear characteristics of the muscles and the motor control architecture that can control motion and exerted force independently. Mechanical impedance (i.e. stiffness, viscosity and inertia) constitutes the most solid characteristic for describing the dynamic behavior of human movements. This paper presents a method for estimating upper limb impedance characteristics in the three-dimensional (3D) space, covering a wide range of the arm workspace. While subjects maintained postures, a seven-degrees-of-freedom (7-DoFs) robot arm was used to produce small displacements of subjects' hands along the three Cartesian axes. The end-point dynamic behavior was modeled using a linear second-order system and the impedance characteristics in the 3D space were identified using the measured forces and motion profiles. Experimental results were confirmed with two subjects.**

I. Introduction

Applications of robots that are in full contact interaction with humans has received increased attention during the last decades. Since the late 80's, there has been a substantial amount of interest in measuring human arm end-point two-dimensional (2D) stiffness characteristics, with the arm vertically supported and constrained to movement within a horizontal plane. In [1], a perturbation method to measure hand stiffness was developed, by using a manipulandum to displace the subject's hand during maintenance of a given posture. Stiffness values were represented both numerically and graphically as ellipses and it was shown that the end-point dynamic characteristics were mainly composed of spring-like elements. A similar technique was used in [2] and [3]. In [4] and [5] the perturbation method was extended to include measurement of dynamic components such as viscosity and inertia, as well as stiffness.

However, all previous studies focused only on arm motion at the horizontal plane. This essentially restricts the generalization of the results and the use of the respective conclusions. A recent study [6] attempted to identify end-point impedance characteristics in the three-dimensional (3D) space by using a non-parametric method. However, stochastic methods are not able to provide insight of the neuromuscular systems and its interaction with the environment. Therefore, a systematic method for studying the dynamic characteristics of the arm in the 3D space is required. Such a method can provide significant information of the impedance of the upper limb across a larger part of the available workspace, and illustrate how the already analyzed properties of the arm impedance in the horizontal plane can generalize (if possible) to the 3D space.

In this paper, a systematic method for characterizing the arm impedance in the 3D space is presented. A seven-degrees-of-freedom (7-DoFs) robot manipulator equipped with a six-axis force-torque sensor at its end-effector, is used in order to impose motion and measure interaction forces with a subject's hand. The subject's hand is appropriately attached at the robot's end-effector. The manipulator imposes small displacements at the subject's hand, along the three axes, starting at various points in the 3D space throughout the arm workspace. The displacements follow specifically programmed trajectories with varying speed, in order to study the dynamic behavior of the subject's arm. A simplified linear model for hand impedance is used and inertia, viscosity and stiffness characteristics are computed from the available measurements of motion and force. Moreover, using a magnetic position tracking system, the upper limb joint angles are also recorded. The resulted characteristics are graphically represented using ellipsoids and therefore the dynamic behavior of the arm in 3D space is directly assessed.

II. Materials and Methods

The goal of this study was to develop a method for measuring the dynamic characteristics of the human arm end-point in the 3D space. These properties were analyzed in multiple points in the 3D space sufficiently covering the arm workspace. The method followed is based on the motion perturbation during maintained posture of the arm [1], but extended through two main features; the motion perturbation was not with constant velocity but dynamic, i.e. had varying velocity profile. In addition, the arm was perturbed with motion in the 3D space and not only on the horizontal plane. Using these two new characteristics, full 3D arm impedance characteristics could be identified and not 2D values of arm stiffness only as in previous works ([1], [7], [5]). Finally, a graphical representation of arm impedance in space was introduced.

This work has been partially supported by the European Commission with the Integrated Project no. 248587, "THE Hand Embodied", within the FP7-ICT-2009-4-2-1 program "Cognitive Systems and Robotics".

P. K. Artemiadis is with the Department of Mechanical Engineering, Massachusetts Institute of Technology (MIT), Cambridge, MA, USA. Email: partem@mit.edu.

P. T. Katsiaris, M. V. Liarokapis and K. J. Kyriakopoulos are with the Control Systems Lab, School of Mechanical Eng., National Technical University of Athens, 9 Heroon Polytechniou Str, Athens, 157 80, Greece. Email: pkatsiar@mail.ntua.gr, mliaro@mail.ntua.gr, kkyria@mail.ntua.gr.

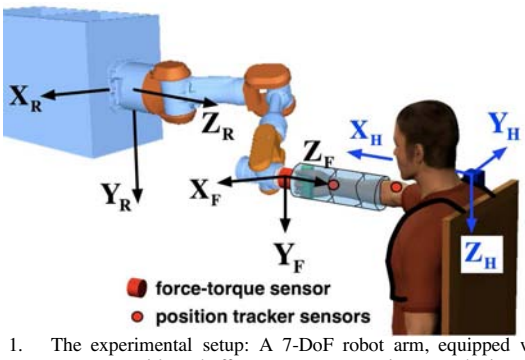

Fig. 1. The experimental setup: A 7-DoF robot arm, equipped with a force-torque sensor at it's end-effector generates motion perturbations to the human arm, through the tube-handle system shown. The user has his forearm inserted in the tube, secured with transversal straps, while he is constantly holding the handle at the end of the tube. The tube is firmly connected with the force-torque sensor. Position tracker sensors are placed at the shoulder and the wrist of the user, while the reference system is attached on the shoulder of the user. $\mathbf{X_R}$, $\mathbf{Y_R}$, $\mathbf{Z_R}$ are the robot reference frame axes. $\mathbf{X_H}$, $\mathbf{Y_H}$, $\mathbf{Z_H}$ are the human (or position tracker) reference frame axes. $\mathbf{X_F}$, $\mathbf{Y_F}$, $\mathbf{Z_F}$ are the force-torque sensor reference frame axes. The user's torso is firmly supported at a flat surface to prevent body movements during the experiment.

A. Apparatus

Subjects were seated with their trunk restrained to the chair through harness belt. The subjects gripped an appropriately designed handle, mounted on the robot end-effector, with their dominant arm. The handle was inside a tube, in which the subject's forearm was inserted. The subjects' forearm was supported inside the tube through elastic straps transversely inserted into the tube. The tube was appropriately designed so that it restrained wrist motion (wrist flexion-extension and radial-ulnar deviation). The subjects were instructed to always hold the handle firmly. The handle-tube along with the subjects' hand is graphically depicted in Fig. 1. The tube-handle system was mounted on a 7-DoF robot manipulator (PA-10, Mitsubishi Heavy Industries). Further information for hardware characteristics, kinematics and dynamics can be found in [8]. Between the tube-handle mounting and the robot end-effector, a 6-axis force-torque sensor (JR3 Inc.) was included for measuring human-robot interaction forces in the three axes of space. The subjects were seated so that most of their arm workspace was accessible from the robot workspace.

A magnetic position tracking system (Isotrak II, Polhemus Inc) was used for measuring the human arm configuration. The position tracking system was equipped with a base reference system, with respect to which, the 3D-position and orientation of two small position sensors is given in real-time. The position sensors were firmly attached at the elbow (at the olecranon) and the wrist (at the styloid process of radius) of the subject, while the reference system was placed on the subjects' shoulder as shown in Fig. 1. The axes of the robot arm and position tracking system were properly aligned during a calibration procedure, using online measurements of both systems. Let $\mathbf{X_R}$, $\mathbf{Y_R}$, $\mathbf{Z_R}$ be the robot reference axes vectors, and let $\mathbf{X_H}$, $\mathbf{Y_H}$, $\mathbf{Z_H}$ be the human references axes vectors (i.e. the position tracking system base). Then, the relationship between them, as shown in Fig. 1, is defined by

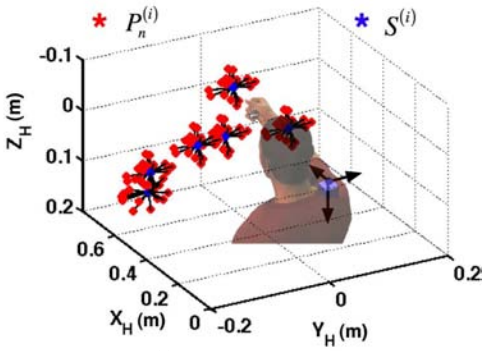

Fig. 2. Starting points, $S^{(i)},\ i = 1, 2, \ldots, 6$, and corresponding target points, $P_n^{(i)},\ n = 1, 2, \ldots, 16$, for end-point perturbation in the 3D arm workspace.

$$\left[\ \mathbf{X_R} \quad \mathbf{Y_R} \quad \mathbf{Z_R}\ \right] = \left[\ -\mathbf{Y_H} \quad \mathbf{Z_H} \quad -\mathbf{X_H}\ \right] \quad (1)$$

B. Procedures and Tasks

Two subjects participated at the experiments. Each subject was asked to firmly hold the handle while looking towards the robot arm, as shown in Fig. 1. The robot arm end-effector was initially positioned at six starting 3D points ($S^{(i)},\ i = 1, 2, \ldots, 6$), inside the human arm workspace. More specifically, the starting points belonged to a sphere of radius 20 cm and center a point chosen as the center of studied arm workspace. Starting for each point $S^{(i)}$, the robot end-effector was moved to 16 surrounding points $P_n^{(i)},\ n = 1, 2, \ldots, 16$, that belonged to a sphere with center the point $S^{(i)}$ and radius equal to 3 cm. All the points and motion paths are depicted in Fig. 2.

The robot end-effector initiated the motion from each point $S^{(i)},\ i = 1, 2, \ldots, 6$, to each point $P_n^{(i)},\ n = 1, 2, \ldots, 16$, lasting for 3 seconds (*center-out phase*). After arriving at point $P_n^{(i)}$, the robot stayed there for 2 seconds (*relax phase 1*), and then returned to the starting point $S^{(i)}$ following a constant velocity line path taking 2 seconds (*return phase*). Finally the robot end-effector stayed there for 2 seconds (*relax phase 2*), before initiating motion for the next $P_n^{(i)}$ point. The subjects were instructed to try to maintain their hand initial position $S^{(i)}$ only during the *center-out phase*, i.e. trying to restrain to robot center-out motion. During all the other phases (*relax phase 1* and *2*, and *return phase*) the subjects were instructed to relax and passively follow robot induced motion.

The perturbed motion coming from the robot end-effector motion during the *center-out phase* was specifically designed as dynamic. Three kinds of trajectories along each axis were designed; polynomial (3^{rd} order), trapezoidal and sinusoidal. The polynomial trajectory was designed so that the motion at each axis was described by a 3^{rd} order polynomial, with zero initial and final velocity, resulting to smooth initiation and termination of robot motion. The trapezoidal trajectory was defined with a trapezoidal profile for velocity at each axis of motion, i.e. constant velocity throughout the motion (i.e.

the *center-out phase*), except from the first and last 10% of the motion allowing for proper acceleration and deceleration. During the latter periods, the velocity was linearly changing. The sinusoidal trajectory was designed so that the robot end-effector was performing two full-periods of sinusoidal oscillations around the initial point $S^{(i)}$ along each axis of motion. The amplitude of the sinusoidal motion was equal to the distance between the initial point $S^{(i)}$ and the target point $P_n^{(i)}$, while the duration of sinusoidal motion was six seconds, succeeded by a 3 seconds resting period.

Therefore, the 3D position of the robot end-effector was defined by the different kinds of trajectories. Regarding the orientation, the robot end-effector was controlled to have all orientation angles (roll, pitch and yaw) equal to zero. This essentially guaranteed that the tube-handle system would keep a constant orientation with respect to the subject, which was identical to the initial one, as shown in Fig. 1[3]. Having the desired pose of the robot end-effector, the appropriate robot joint angles were computed using the pseudo-inverse Jacobian method [9]. For details on this procedure, the reader can refer to [8]. All the robot trajectories were designed and computed offline. Having computed the desired robot trajectories in joint space, the robot could be commanded to track those trajectories using its high-performance servo controller, with a maximum tracking error in joint space that did not exceed 0.02 deg. Finally, the force-torque sensor was mounted on the robot end-effector, while its axes were aligned to those of the robot, as shown in Fig. 1.

Each of the two subjects (2 males of 25 and 26 years old) completed the experimental session including the 16 surrounding target $P_n^{(i)},\ n = 1, 2, \ldots, 16$ for each of the 6 starting points $S^{(i)},\ i = 1, 2, \ldots, 6$ inside their arm workspace. The recording of the data started as soon as the robot end-effector initiated motion from each of the points $S^{(i)},\ i = 1, 2, \ldots, 6$ to its surrounding targets $P_n^{(i)},\ n = 1, 2, \ldots, 16$. For example, if $t = 0$ is when the robot initiated motion from point $S^{(1)}$ to each one of its 16 surrounding targets $P_1^{(1)}$, $P_1^{(2)}$, ..., $P_1^{(16)}$, then the experiment stops after 16 motions from $S^{(1)}$ to each $P_n^{(1)},\ n = 1, 2, \ldots, 16$ and back to $S^{(1)}$, lasting eventually $t = 9 * 16 = 144sec$. Then the robot was moved to the next initial point (i.e. $S^{(2)}$) and the next session was started as soon as the subject confirmed that he was ready after resting his arm. All experimental procedures were conducted under a protocol approved by the National Technical University of Athens Institutional Review Board.

C. Data Processing

As described above, data were sampled at the frequency of 500 Hz and stored for offline analysis. Data include robot arm joint angles, force-torque sensors measurements including forces along the $\mathbf{X_F}$, $\mathbf{Y_F}$, $\mathbf{Z_F}$ axes (as shown in Fig. 1), and position and orientation of the two position tracker sensors placed on the human arm. Regarding the robot end-effector position, it was computed using the forward kinematics equations of the robot, from the recorded joint angles. Details on the kinematics can be found in [8]. As for the human end-point position, this was monitored through the second position tracker, with respect to the tracker base reference system $\langle \mathbf{X_H}, \mathbf{Y_H}, \mathbf{Z_H} \rangle$.

Regarding force measurements, the initial force values for each axis were subtracted from all the acquired measurements. This was done at the initiation of each individual motion, so to ensure that all measurements offsets due to sensor calibration, or misalignments, and human arm weight gravitational forces were not affecting the force measurements. Since the motion from the starting points $S^{(i)}$ was limited in terms of distance covered and velocity, while the human arm configuration changes were also small, the gravitation forces were considered constant.

1) Modeling arm impedance: Since the displacement of the subject's hand from the starting point (maintained posture) was small, the hand impedance model can be expressed in the end-point level when the human arm is under a stable posture, by the following equation:

$$\mathbf{M_e}\ddot{\mathbf{X}} + \mathbf{B_e}\dot{\mathbf{X}} + \mathbf{K_e}\left(\mathbf{X} - \mathbf{X_u}\right) = \mathbf{F} \tag{2}$$

where $\mathbf{M_e}$, $\mathbf{B_e}$, $\mathbf{K_e} \in \mathbb{R}^{3\times3}$ represented the hand inertia, viscosity and stiffness matrices respectively, $\mathbf{X} \in \mathbb{R}^3$ and $\mathbf{F} \in \mathbb{R}^3$ represented the end-point position and force vectors with respect to the human reference system $\langle \mathbf{X_H}, \mathbf{Y_H}, \mathbf{Z_H} \rangle$, while $\mathbf{X_u}$ represented the virtual equilibrium position of the stiffness component. Eq. (2) was used for modeling local end-point impedance, since within small displacements linearity could be assumed ([1], [6], [10]). Finally Coriolis terms are discarded as second order effects in the linearization.

2) Identification of arm impedance: Since the experiments were of maintaining arm posture, the force vector $\mathbf{F}$ in (2) was equal in magnitude and of opposite direction of the force vector measured by the force-torque sensor. Moreover, the end-point position vector $\mathbf{X}$ was available (both from the robot end-effector position and the position tracker measurements as noted above). Therefore, eq. (2) was transformed to an identifiable form, with respect to the impedance matrices $\mathbf{M_e}$, $\mathbf{B_e}$, $\mathbf{K_e}$, as shown below:

$$\mathbf{Y}\pi = \mathbf{F} \tag{3}$$

where $\pi \in \mathbb{R}^{27}$ was the parameter vector to be identified, given by

$$\begin{aligned}\pi = \big[\ & \mathbf{M}_{\mathbf{e_x}}^T \quad \mathbf{B}_{\mathbf{e_x}}^T \quad \mathbf{K}_{\mathbf{e_x}}^T \quad \mathbf{M}_{\mathbf{e_y}}^T \\ & \mathbf{B}_{\mathbf{e_y}}^T \quad \mathbf{K}_{\mathbf{e_y}}^T \quad \mathbf{M}_{\mathbf{e_z}}^T \quad \mathbf{B}_{\mathbf{e_z}}^T \quad \mathbf{K}_{\mathbf{e_z}}^T\ \big]^T\end{aligned} \tag{4}$$

where

$$\begin{aligned}\mathbf{M_e} &= \left[\ \mathbf{M}_{\mathbf{e_x}} \quad \mathbf{M}_{\mathbf{e_y}} \quad \mathbf{M}_{\mathbf{e_z}}\ \right]^T \\ \mathbf{B_e} &= \left[\ \mathbf{B}_{\mathbf{e_x}} \quad \mathbf{B}_{\mathbf{e_y}} \quad \mathbf{B}_{\mathbf{e_z}}\ \right]^T \\ \mathbf{K_e} &= \left[\ \mathbf{K}_{\mathbf{e_x}} \quad \mathbf{K}_{\mathbf{e_y}} \quad \mathbf{K}_{\mathbf{e_z}}\ \right]^T.\end{aligned} \tag{5}$$

$\mathbf{Y}$ in eq. (3) was a (3×27) matrix defined by

$$\mathbf{Y} = \begin{bmatrix} \mathbf{L}^T & \mathbf{0}_{1\times9} & \mathbf{0}_{1\times9} \\ \mathbf{0}_{1\times9} & \mathbf{L}^T & \mathbf{0}_{1\times9} \\ \mathbf{0}_{1\times9} & \mathbf{0}_{1\times9} & \mathbf{L}^T \end{bmatrix} \tag{6}$$

[3]The tube longitudinal axis was always perpendicular to the coronal plane.

where $\mathbf{L} \in \mathbb{R}^9$ was defined by

$$\mathbf{L} = \left[\begin{array}{ccc} \ddot{\mathbf{X}}^T & \dot{\mathbf{X}}^T & \left(\mathbf{X} - \mathbf{X_u}\right)^T \end{array} \right]^T, \tag{7}$$

and $\mathbf{0}_{1\times 9}$ was a zero matrix of size (1×9), and $\dot{\mathbf{X}}$, $\ddot{\mathbf{X}}$ vectors representing end-point velocity and acceleration. Using eq. (3) for m measurements of the end-point position and force collected during the experiments, the parameter vector π was computed by the least-squares method represented by the following:

$$\pi = \mathbf{Y_a^{\dagger}} \mathbf{F_a} \tag{8}$$

where $\mathbf{Y_a^{\dagger}}$ was the left pseuso-inverse matrix of $\mathbf{Y_a}$, while the matrix $\mathbf{Y_a} \in \mathbb{R}^{3m\times 27}$ and the vector $\mathbf{F_a} \in \mathbb{R}^{3m}$ were formed by concatenating m instances of $\mathbf{Y}$ and $\mathbf{F}$ respectively, according to eq. (3), corresponding to the m measurement points during the experiments. I.e.

$$\mathbf{Y_a} = \left[\begin{array}{ccc} \mathbf{L}_1^T & \mathbf{0}_{1\times 9} & \mathbf{0}_{1\times 9} \\ \mathbf{0}_{1\times 9} & \mathbf{L}_1^T & \mathbf{0}_{1\times 9} \\ \mathbf{0}_{1\times 9} & \mathbf{0}_{1\times 9} & \mathbf{L}_1^T \\ \vdots & \vdots & \vdots \\ \mathbf{L}_m^T & \mathbf{0}_{1\times 9} & \mathbf{0}_{1\times 9} \\ \mathbf{0}_{1\times 9} & \mathbf{L}_m^T & \mathbf{0}_{1\times 9} \\ \mathbf{0}_{1\times 9} & \mathbf{0}_{1\times 9} & \mathbf{L}_m^T \end{array} \right], \qquad \mathbf{F_a} = \left[\begin{array}{c} \mathbf{F_1} \\ \vdots \\ \mathbf{F_m} \end{array} \right] \tag{9}$$

where $\mathbf{L}_i$, $\mathbf{F}_i$ were instances of $\mathbf{L}$, $\mathbf{F}$ for each data point i, $i = 1, 2, \ldots, m$, according to eq. (7) and (6). Therefore, using the experimental measurements, the impedance matrices $\mathbf{M_e}$, $\mathbf{B_e}$, $\mathbf{K_e}$ in Cartesian space were identified.

3) Impedance analysis: The impedance matrices $\mathbf{M_e}, \mathbf{B_e}, \mathbf{K_e}$ were separated into a symmetric and an antisymmetric component. Generally, if $\mathbf{Z} \in \mathbb{R}^{3\times 3}$ was an impedance matrix, it was separated into a symmetric $\mathbf{Z^{(s)}}$ and an antisymmetric $\mathbf{Z^{(a)}}$ component, i.e.

$$\mathbf{Z} = \left[\begin{array}{ccc} Z_{xx} & Z_{xy} & Z_{xz} \\ Z_{yx} & Z_{yy} & Z_{yz} \\ Z_{zx} & Z_{zy} & Z_{zz} \end{array} \right] = \mathbf{Z^{(s)}} + \mathbf{Z^{(a)}} \tag{10}$$

where

$$\begin{array}{l} \mathbf{Z^{(s)}} = \frac{1}{2}\left(\mathbf{Z} + \mathbf{Z}^T\right) \\ \mathbf{Z}^{(a)} = \frac{1}{2}\left(\mathbf{Z} - \mathbf{Z}^T\right) \end{array} \tag{11}$$

If $f(x, y, z)$ is a differentiable, nonlinear function of the position of the arm end-point, where x, y, z the position of the end-point in the 3D space, it is possible to express the hand impedance as a differential operator that relates small variations of force (dF_x, dF_y, dF_z) with small displacements (dx, dy, dz), i.e.

$$\begin{array}{l} dF_x = \left(\frac{\partial F_x}{\partial x}\right) dx + \left(\frac{\partial F_x}{\partial y}\right) dy + \left(\frac{\partial F_x}{\partial z}\right) dz = \\ \quad Z_{xx}dx + Z_{xy}dy + Z_{xz}dz \\ dF_y = \left(\frac{\partial F_y}{\partial x}\right) dx + \left(\frac{\partial F_y}{\partial y}\right) dy + \left(\frac{\partial F_y}{\partial z}\right) dz = \\ \quad Z_{yx}dx + Z_{yy}dy + Z_{yz}dz \\ dF_z = \left(\frac{\partial F_z}{\partial x}\right) dx + \left(\frac{\partial F_z}{\partial y}\right) dy + \left(\frac{\partial F_z}{\partial z}\right) dz = \\ \quad Z_{zx}dx + Z_{zy}dy + Z_{zz}dz \end{array} \tag{12}$$

The above equation is only correct for small displacements. Therefore, the physical meaning of the symmetric impedance component is that the force field $f(x, y, z)$ is conservative. The antisymmetric component essentially represents the curl of the force field and was generated mainly by the hand [1]. It's contribution to the overall impedance is described in the Results section.

4) Impedance representation: An ellipsoid (see Fig. 3) centered at the origin is represented by the following equation:

$$a_{11}x^2 + a_{22}y^2 + a_{33}z^2 + 2a_{12}xy + 2a_{13}xz + 2a_{23}yz = 1 \tag{13}$$

where a_{11}, a_{22}, a_{33}, a_{12}, a_{13}, a_{23} elements of a symmetric matrix $\mathbf{A} \in \mathbb{R}^{3\times 3}$, i.e.

$$\mathbf{A} = \left[\begin{array}{ccc} a_{11} & a_{12} & a_{13} \\ a_{12} & a_{22} & a_{23} \\ a_{13} & a_{23} & a_{33} \end{array} \right] \tag{14}$$

The principal axes of the ellipsoid $\mathbf{x^{(1)}}$, $\mathbf{x^{(2)}}$, $\mathbf{x^{(3)}} \in \mathbb{R}^3$ are the eigenvectors of the matrix $\mathbf{A}$, and they are all orthogonal to each other. These eigenvectors essentially define the principal reference system of the ellipsoid. Let α, β, γ be the yaw, pitch and roll angles that define the orientation of the principal reference system of the ellipsoid, with respect to the base reference system. The rotation matrix describing the ellipsoid principal reference system with respect to the base system is given by:

$$\mathbf{R}(\alpha, \beta, \gamma) = \mathbf{R_z}(\alpha)\,\mathbf{R_y}(\beta)\,\mathbf{R_x}(\gamma) \tag{15}$$

where $\mathbf{R_x}$, $\mathbf{R_y}$, $\mathbf{R_z}$ follow the standard notation of rotation matrices. Since the eigenvectors of the matrix $\mathbf{A}$ define the orientation of the ellipsoid principal reference system, it is:

$$\mathbf{R}(\alpha, \beta, \gamma) = \left[\begin{array}{ccc} \mathbf{x^{(1)}} & \mathbf{x}^{(2)} & \mathbf{x}^{(3)} \end{array} \right] \tag{16}$$

Solving (16) for the α, β, γ orientation angles it is:

$$\begin{array}{l} \alpha = \tan^{-1}\left(\frac{r_{21}}{r_{11}}\right), \beta = \tan^{-1}\left(\frac{-r_{31}}{\sqrt{r_{32}^2 + r_{33}^2}}\right), \\ \gamma = \tan^{-1}\left(\frac{r_{32}}{r_{33}}\right) \end{array} \tag{17}$$

where $\left[\begin{array}{ccc} \mathbf{x^{(1)}} & \mathbf{x}^{(2)} & \mathbf{x}^{(3)} \end{array} \right] = \left[\begin{array}{ccc} r_{11} & r_{12} & r_{13} \\ r_{21} & r_{22} & r_{23} \\ r_{31} & r_{32} & r_{33} \end{array} \right]$. Moreover, the equatorial radii a, b (along the principal axes $\mathbf{x^{(1)}}$ and $\mathbf{x^{(2)}}$ respectively) and the polar radius c (along the principal axis $\mathbf{x^{(3)}}$) of the ellipsoid are given by: $a = \frac{1}{\sqrt{\lambda_1}}$, $b = \frac{1}{\sqrt{\lambda_2}}$, $c = \frac{1}{\sqrt{\lambda_3}}$, where λ_1, λ_2, λ_3 are the eigenvalues of the matrix $\mathbf{A}$. Based on the above, the symmetric parts $\mathbf{M_e^{(s)}}$, $\mathbf{B_e^{(s)}}$, $\mathbf{K_e^{(s)}}$ of the impedance matrices, were represented with ellipsoids with center the starting points $(S^{(i)},\ i = 1, 2, \ldots, 6)$, radii along their individual principal axes and orientation defined above.

III. Results

The impedance matrices $\mathbf{M_e}$, $\mathbf{B_e}$, $\mathbf{K_e}$ for each starting point S_i per subject were identified as analyzed above, and separated into their symmetric and antisymmetric components. The estimated numerical values of the symmetric

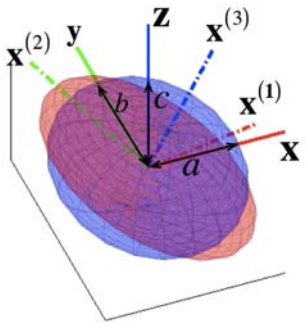

Fig. 3. Ellipsoids principal axes before ($\mathbf{x}$, $\mathbf{y}$, $\mathbf{z}$) and after ($\mathbf{x^{(1)}}$, ($\mathbf{x^{(2)}}$, $\mathbf{x^{(3)}}$) rotation of α, β, γ (see (17)). The equatorial radii a, b (along the principal axes $\mathbf{x^{(1)}}$ and $\mathbf{x^{(2)}}$ respectively) and the polar radius c (along the principal axis $\mathbf{x^{(3)}}$) of the ellipsoid are shown.

components of each impedance matrix are shown in Table I. The corresponding values of the non-symmetric impedance components were observed to be much lower than the corresponding ones in the symmetric impedance components. Table II compares the values of non-symmetric and symmetric impedance components. The terms with subscripts max, min, denote the maximum and minimum values of the corresponding symmetric impedance components, while the terms with subscript max_A denote the maximum difference between the off-diagonal symmetric elements of the antisymmetric impedance component matrices. As it is shown, the contribution of the curl of the force field (i.e. the non-symmetric impedance components, see Section II) was identified as very low. Finally it must be noted that the values of arm impedance were identified after the application of the least square method analyzed in Section II, while the correlation coefficients between the recorded force values and the ones computed using the fitted model parameters, were 0.94, 0.88 and 0.87 for the 3 Cartesian axes of motion respectively.

As discussed in Section II, the impedance components can be represented by ellipsoids. In Fig. 4, the ellipsoids of each of the impedance components, i.e. stiffness, viscosity and inertia are depicted. As it can be shown, the stiffness components are the ones that prevail compared to the viscosity and inertial components, a result that is consistent with previous studies in the 2D space [1], [3].

IV. Conclusions and discussion

In this paper, the impedance characteristics of the human upper limb in the 3D space was analyzed. First, an experimental protocol was defined to study the dynamic characteristics of the arm impedance in the 3D space. Then, experimental data were fitted to a model defined for the 3D arm impedance. The main novelty of this work is the expansion of all the previous studies of arm impedance to the 3D space. Since every-day life tasks demand the movement of the upper limb in the 3D Cartesian space, the modeling and characterization of the arm impedance in this space is significant. Finally, a way of representing the impedance components was introduced and applied to the experimental

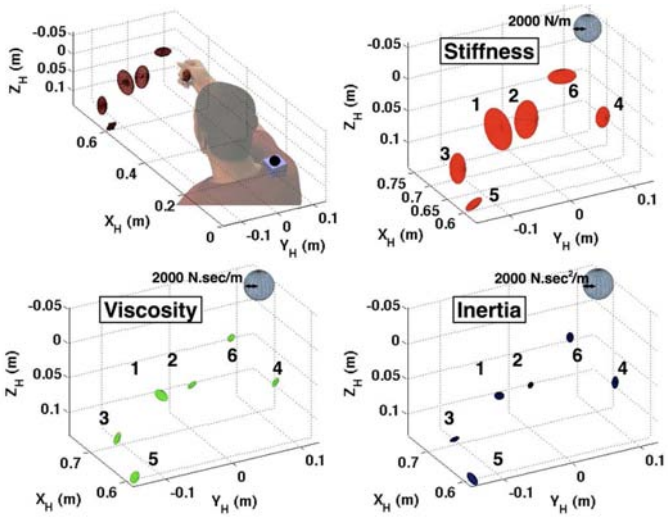

Fig. 4. Representation of impedance characteristics in the 3D arm workspace. Top left figure: impedance ellipsoids centered in the points measured in the arm workspace. Top right and bottom figures: enlarged image of stiffness, viscosity and inertia components of the arm impedance represented by ellipsoids. The scale of the figures in shown at the top right corner of each one, where a sphere of a radius representing the noted value is shown. Number of points are shown in top right figure, where each point i corresponds to the starting point $S^{(i)}$, $i = 1, 2, \ldots, 6$.

data. The significance of the characterization of the 3D arm impedance can be found in many fields. In the field of robotics, advanced control schemes for orthotic devices (i.e. arm exoskeletons) can be developed and implemented, based on arm impedance characteristics.

References

[1] F. A. Mussa-Ivaldi, N. Hogan, and E. Bizzi, "Neural, mechanical, and geometric factors subserving arm posture in humans," *J Neurosci*, pp. 2732–2743, 1985.

[2] T. Tsuji and M. Kaneko, "Human arm stiffness and equilibrium-point trajectory during multi-joint movement," *Biol. Cybern.*, vol. 76, pp. 163–171, 1997.

[3] E. Burdet, R. Osu, D. W. Franklin, T. Yoshioka, T. E. Milner, and M. Kawato, "A method for measuring endpoint stiffness during multi-joint arm movements," *Journal of Biomechanics*, vol. 33, pp. 1705–1709, 2000.

[4] J. M. Dolan, M. B. Friedman, and M. L. Nagurka, "Dynamic and loaded impedance components in the maintenance of human arm posture," *IEEE Trans Sys Man Cybern*, vol. 23, pp. 698–709, 1993.

[5] T. Tsuji, P. G. Morasso, K. Goto, and K. Ito, "Human hand impedance characteristics during maintained posture," *Biol Cybern*, pp. 475–485, 1995.

[6] M. C. Pierre and R. F. Kirsch, "Measuring dynamic characteristics of the human arm in three dimensional space," *Proceedings of the Second Joint EMBS/BMES Conference*, vol. 3, pp. 2558–2560, 2002.

[7] T. Flash and F. A. Mussa-Ivaldi, "Human arm stiffness characteristics during the maintenance of posture," *Exp Brain Res*, pp. 315–326, 1990.

[8] N. A. Mpompos, P. K. Artemiadis, A. S. Oikonomopoulos, and K. J. Kyriakopoulos, "Modeling, full identification and control of the mitsubishi PA-10 robot arm," *Proc. of IEEE/ASME International Conference on Advanced Intelligent Mechatronics, Switzerland*, 2007.

[9] L. Sciavicco and B. Siciliano, *Modeling and control of robot manipulators*. McGraw-Hill, 1996.

[10] Y. Takeda, Y. Tanaka, and T. Tsuji, "Impedance simulator: Analysis of human hand impedance characteristics," *Proceedings of the second International Symposium on Measurement, Analysis and Modeling of Human Functions*, 2004.

TABLE I

ESTIMATED SYMMETRIC COMPONENTS OF THE ARM IMPEDANCE IN 3D SPACE

Subject	Hand position	Stiffness $\left(\frac{N}{m}\right)$			Viscosity $\left(\frac{N\,\mathrm{sec}}{m}\right)$			Inertia $\left(\frac{N\,\mathrm{sec}^2}{m}\right)$		
		$K^{(s)}_{e_{xx}}$	$K^{(s)}_{e_{xy}}$	$K^{(s)}_{e_{xz}}$	$B^{(s)}_{e_{xx}}$	$B^{(s)}_{e_{xy}}$	$B^{(s)}_{e_{xz}}$	$M^{(s)}_{e_{xx}}$	$M^{(s)}_{e_{xy}}$	$M^{(s)}_{e_{xz}}$
		$K^{(s)}_{e_{yx}}$	$K^{(s)}_{e_{yy}}$	$K^{(s)}_{e_{yz}}$	$B^{(s)}_{e_{yx}}$	$B^{(s)}_{e_{yy}}$	$B^{(s)}_{e_{yz}}$	$M^{(s)}_{e_{yx}}$	$M^{(s)}_{e_{yy}}$	$M^{(s)}_{e_{yz}}$
		$K^{(s)}_{e_{zx}}$	$K^{(s)}_{e_{zy}}$	$K^{(s)}_{e_{zz}}$	$B^{(s)}_{e_{zx}}$	$B^{(s)}_{e_{zy}}$	$B^{(s)}_{e_{zz}}$	$M^{(s)}_{e_{zx}}$	$M^{(s)}_{e_{zy}}$	$M^{(s)}_{e_{zz}}$
1	$S^{(1)}$	1002	12	26	86	22	25	0.40	0.03	0.02
		12	250	94	22	56	9	0.03	0.35	0.01
		26	94	320	25	9	47	0.02	0.01	0.19
	$S^{(2)}$	620	208	86	139	16	15	0.16	0.02	0.01
		208	360	83	16	18	11	0.02	0.03	0.01
		86	83	449	15	11	17	0.01	0.01	0.18
	$S^{(3)}$	429	155	42	32	17	21	0.22	0.02	0.07
		155	181	44	17	25	16	0.02	0.36	0.12
		42	44	221	21	16	61	0.07	0.12	0.11
	$S^{(4)}$	224	55	9	21	14	12	0.60	0.03	0.08
		55	67	16	14	18	4	0.03	0.14	0.01
		9	16	167	12	4	35	0.08	0.01	0.18
	$S^{(5)}$	431	52	23	96	2.2	8.1	0.24	0.22	0.07
		52	72	41	2.2	12	1.5	0.11	0.63	0.32
		23	41	68	1.5	8.1	41	0.07	0.32	0.47
	$S^{(6)}$	690	75	21	55	8.2	5.58	0.31	0.08	0.05
		75	282	60	8.2	18	6.68	0.08	0.22	0.06
		21	60	117	5.58	6.68	20	0.05	0.06	0.31
2	$S^{(1)}$	1032	182	230	110	12	13	0.12	0.02	0.07
		182	351	148	12	86	9.5	0.02	0.15	0.03
		230	148	544	13	9.5	89	0.07	0.03	0.09
	$S^{(2)}$	879	250	65	64	17	15	0.45	0.14	0.17
		250	334	103	17	28	19	0.14	0.28	0.03
		65	103	271	15	19	58	0.17	0.03	0.22
	$S^{(3)}$	1068	218	253	114	6.1	18	0.71	0.08	0.07
		218	647	258	6.1	28	3.5	0.08	0.39	0.50
		253	258	803	18	3.5	22	0.07	0.50	0.23
	$S^{(4)}$	741	89	141	47	15	4	0.75	0.07	0.06
		89	506	235	15	49	1.7	0.07	0.31	0.05
		141	235	320	4	1.7	24	0.06	0.05	0.51
	$S^{(5)}$	1072	86	177	203	4.5	6.8	0.32	0.05	0.03
		86	640	56	4.5	68	4.1	0.05	0.31	0.03
		177	56	214	6.8	4.1	44	0.03	0.03	0.28
	$S^{(6)}$	791	54	25	42	8.4	5.7	0.37	0.07	0.03
		54	352	52	8.4	17	3.2	0.07	0.18	0.15
		25	52	138	5.7	3.2	23	0.03	0.15	0.19

TABLE II

ANTISYMMETRIC AND SYMMETRIC COMPONENTS OF THE ARM IMPEDANCE IN 3D SPACE

Subject	Hand position	Stiffness $\left(\frac{N}{m}\right)$			Viscosity $\left(\frac{N\,\mathrm{sec}}{m}\right)$			Inertia $\left(\frac{N\,\mathrm{sec}^2}{m}\right)$		
		$K^{(s)}_{e_{max}}$	$K^{(s)}_{e_{min}}$	$K^{(s)}_{e_{max_A}}$	$B^{(s)}_{e_{max}}$	$B^{(s)}_{e_{min}}$	$B^{(s)}_{e_{max_A}}$	$M^{(s)}_{e_{max}}$	$M^{(s)}_{e_{min}}$	$M^{(s)}_{e_{max_A}}$
1	$S^{(1)}$	1002	12	2	86	9	1	0.40	0.01	1.3e-3
	$S^{(2)}$	620	83	13	139	11	2	0.18	0.01	2.3e-4
	$S^{(3)}$	429	42	8	61	16	2	0.36	0.02	3.4e-3
	$S^{(4)}$	224	9	2	35	4	0.7	0.60	0.01	1.5e-3
	$S^{(5)}$	431	23	2.3	96	1.5	0.09	0.63	0.07	8.9e-3
	$S^{(6)}$	690	21	1.2	55	5.58	0.17	0.31	0.05	0.01
2	$S^{(1)}$	1032	148	17	110	9.5	1.2	0.15	0.02	2.9e-3
	$S^{(2)}$	879	65	9.3	64	15	1.3	0.45	0.03	3.8e-3
	$S^{(3)}$	1068	218	14	114	3.5	0.08	0.71	0.07	0.01
	$S^{(4)}$	741	89	7.5	49	1.7	0.08	0.75	0.05	8.6e-3
	$S^{(5)}$	1072	56	12	203	4.1	0.9	0.32	0.03	1.9e-3
	$S^{(6)}$	791	25	3.4	42	3.2	0.12	0.37	0.03	1.2e-3